PROCEEDINGS, Thirty-Eighth Workshop on Geothermal Reservoir Engineering
Stanford University, Stanford, California, February 11-13, 2013
SGP-TR-198

ANALYSIS OF MULTISCALE POROSITY AT THE COSO GEOTHERMAL FIELD

Lawrence M. Anovitz[1],
David R. Cole[2],
David D. Faulder[3],
Julie Sheets[2],
Hsiu-Wen Wang[1],
Gernot Rother[1],
Matthew Wasbrough[4],
Rex Hjelm[5],
Monika Hartl[5],
Vitaliy Pipich[6],
Zhensdong Fu[6]

[1] MS 6110, PO Box 2008, Bldg 4100, Oak Ridge National Laboratory, Oak Ridge, TN 37831-6110
anovitzlm@ornl.gov, rotherg@ornl.gov, wangh3@ornl.gov
[2] School of Earth Sciences, 275 Mendenhall Laboratory, 125 South Oval Mall, Ohio State University, Columbus, Ohio, 43210 cole.618@osu.edu, sheets.2@osu.edu
[3] Consultant, Littleton, Colorado 80120 ddfaulder@earthlink.net
[4] NIST Center for Neutron Research, 100 Bureau Drive, stop 8562, Gaithersburg, Maryland 20899-8562
Matthew.Wasbrough@nist.gov
[5] MS H805 Los Alamos National Laboratory, Los Alamos, NM 87545
hjelm@lanl.gov, hartl@lanl.gov
[6] JCNS@FRMII c/o TU Muenchen, Lichtenbergstr.1 85747 Garching, Germany
v.pipich@fz-juelich.de, <z.fu@fz-juelich.de>

ABSTRACT

The multiscale pore structure of the rocks making up a geothermal reservoir and the mineralogy associated with those pores are critical factors for estimating a number of reservoir properties including fluid mass in place, permeability, and capillary pressures as well as geochemical and thermal interactions between the rock and the fluid. This paper describes the results of a combined neutron scattering and imaging analysis of samples from a well on the east flank of the Coso reservoir in California and delineates the close relationship between alteration mineralogy and multiscale porosity.

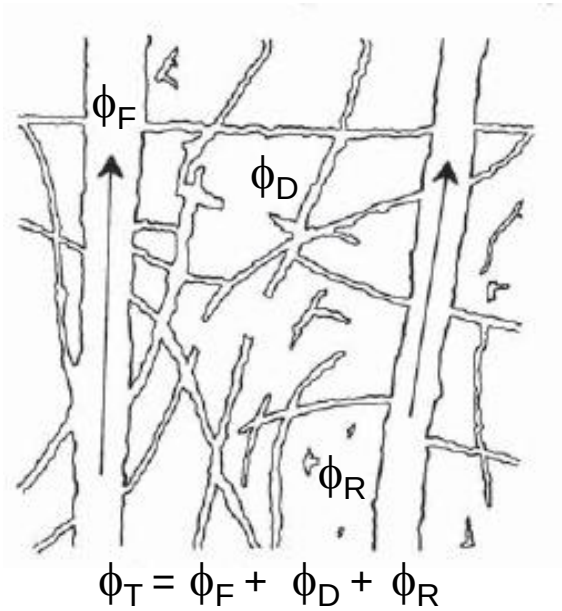

Figure 1: Schematic diagram of possible pore types in geological media (after Norton and Knapp, 1977). See text for explanation

INTRODUCTION

A number of interrelated properties control the amount of heat resource in the earth's crust that can be extracted from the target reservoir rock

including temperature gradient, natural porosity and permeability, rock physical properties (e.g., elastic, brittle, thermal), the stress regime, indigenous stored water and susceptibility to seismicity (e.g., Ingebritsen and Sanford, 1998; Ague, 2004; DOE-EGS, 2006). These factors, taken together, not only control the physical processes of extracting heat, but also play a major role in determining the economics of producing energy. While solid rock is excellent for storing heat, the rate of heat removal by conduction is slow, due to its low thermal conductivity. Hence, only that fraction of the rock volume accessible via natural fractures and pores or made accessible by Enhanced Geothermal Systems (EGS) stimulation can be considered part of the 'active' reservoir where heat extraction occurs. Rocks with at least some connected permeability through fractures or pore spaces are more likely to result in a connected circulation system after stimulation (hydraulic or chemically induced). The fracture/pore network needs to not only be connected but also allow injected fluids sufficient residence time to contact hot rock. However, too much pre-existing porosity and associated permeability and/or enhanced permeability via stimulation could lead to 'short circuits' where fluids move too rapidly from injection wells to the production wells without heating up enough to be economic (DOE-EGS, 2006).

The interface between the circulating geothermal fluid and potentially reactive mineral phases is defined by the relative distribution of solution filled pores and fractures. Coupled processes occurring at this interface transport thermal and mechanical energy, fluid mass, momentum, and chemical components through the porous rock that comprises the geothermal system (e.g., Norton and Knapp, 1977; Norton, 1979). The pore environment in geologic media is composed of several types of pores (see **Fig. 1**). Flow porosity, ϕ_F, includes continuous pores, the principle flow channels. These are usually continuous fractures or pore networks that have relatively large effective apertures or diameters, respectively. Diffusion porosity, ϕ_D, includes discontinuous fractures, pores and grain boundary microcracks which are interconnected to flow pores. Transport of components through these pores occurs primarily by aqueous diffusion. Residual porosity, ϕ_R, includes those pores not connected to either flow or diffusion pores. Total porosity, ϕ_T is the sum of all of these pore types. Studies of paleo-geothermal systems suggest most of the total porosity is in the form of residual pores – i.e., the micro-environment (e.g., Norton, 1979). The goal of the EGS stimulation process is to create more flow porosity while at the same time enhancing diffusion porosity and creating enhanced fracture complexity to access the residual pores, thereby leading to a system with overall greater 'interfacial' surface area to extract heat.

As illustrated in **Fig. 1**, porosity and permeability are key variables that link the thermal, hydrologic, geomechanical and geochemical behavior exhibited by hydrothermal systems in response to the disequilibrium state imposed by perturbations such as injection of water, CO_2 or other 'working' fluids. In general there is a strong positive correlation between these two quantities in many porous and fractured geologic media (Ingebritsen and Sanford, 1998). However, some important classes of geologic media do not adhere to this 'rule-of-thumb' including clays, clay-rich materials and volcanic tuffs. State-of-the-art reactive transport simulators require robust numerical methods that approximate and discretize the coupled mathematical models that account for fluid-rock interactions (Johnson et al. 2004). Among the current limitations of these models, four in particular relate directly to our lack of fundamental understanding of the pore regime critical for geothermal development: (a) the lack of an accurate description of the pore and fracture network; (b) a poor understanding of the extent of pore connectivity; (c) inability to predict the migration of geothermal fluids through the fracture/pore environment over variable length scales; and (d) little or no constraint on how porosity and permeability evolve over time during water-rock interaction (e.g., Deutch, 2007). The microstructure of pore/fracture space in rocks and its evolution during reaction with fluids, where most of the total porosity resides, are critically important factors controlling the distribution of fluid-accessible pore volume, fluid flow dynamics, selective fluid retention by capillary forces, and chemical reactivity at the interface. However, a quantitative understanding of the porosity regime illustrated in **Fig. 1** (i.e., pore size, shape,

and volume, pore size distribution, pore connectivity, pore wall roughness) in fractured rocks is not well established.

This paper describes the results of neutron scattering and mineral mapping analysis as a function of depth of samples from a well from the East flank of the Coso Geothermal field. The data provide quantitiative analysis of the pore structure of these samples from the nanometer to the 10's of microns length scale, and an analysis of the mineralogy at micron scales associated with changes in the observed pore structures.

THE COSO GEOTHERMAL FIELD

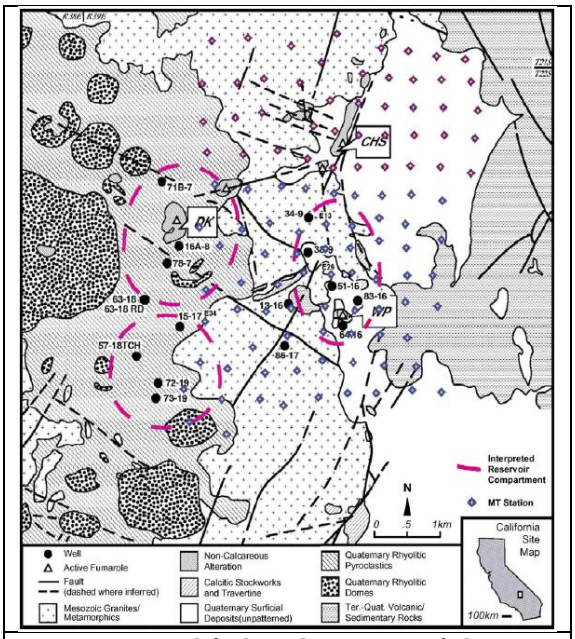

Figure 2: Simplified geologic map of the Coso geothermal field from Newman et al. (2008). The red dashed lines show the interpreted reservoir compartment-talization (Adams et al., 2000, Whitmarsh, 2002. The main alteration areas are Devil's Kitchen (DK), Coso Hotsprings (CSH) and Wheeler Prospect (WP)

Fig. 2 shows a simplified geologic map of the Coso geothermal field (map and description below after Newman et al., 2008). The field is located in the Coso Range in southeastern California at the boundary between the Sierra Nevada and the Basin and Range, and lies within the Walker Lane/Eastern California Shear Zone. The basement is dominated by fractured Mesozoic plutonic rocks intruded by NW trending, fine-grained dikes. It is partly covered by Late Cenozoic volcanics. These dikes range in composition from felsic to mafic and are believed to be part of the Cretaceous Independence Dike swarm. The Late Cenozoic volcanics consist of basalts and rhyolites. 39 rhyolite domes were emplaced in the last million years in the central region of the field along with a relatively small amount of basalt on the margins. Over the past 600,000 years, the depth from which the rhyolites erupted has decreased, ranging from 10 km depth for the 0.6 Ma magma, to 5.5 km for the youngest (0.04 Ma) magma. These results can be explained by either a single rhyolitic reservoir moving upward through the crust, or a series of successively shallower reservoirs, consistent with the recent Ar–Ar geochronology (Kurilovitch et al., 2003). Shallowing of the magma reservoir has resulted in both more frequent and more voluminous eruptions (Manley and Bacon, 2000), and this magma chamber is the likely heat source for the geothermal system. Faulting and fracture permeability is believed to be due to the position of the Coso Range between Basin and Range extensional tectonics to the east and strike-slip tectonics to the west (Roquemore, 1980; McClusky et al., 2001). Two major fault orientations control the geothermal system. The first strike WNW, have a vertical dip, and strike-slip earthquake solutions, while the other strikes NNE and dips to the east. These fault zones have been successfully targeted in the development of the Coso geothermal field, in particular in the east flank area where wells drilled with a steep westerly dip have been the most productive (e.g. Sheridan et al., 2003). The east flank area at depth is a separate thermal system, with age dating of hot spring deposits associated with east flank faulting estimated to be less than 10 kya, suggesting a younger age than the main Coso reservoir. Permeability is high within three individual Coso reservoirs but low in most of the surrounding rock, limiting reservoir fluid recharge and making reinjection important for sustained productivity.

Samples Analyzed

Samples were obtained from four wells from the Coso geothermal field. These are well cuttings, (**Fig. 3**) and samples were taken every 1000 feet

from surface to TD (total depth). The following

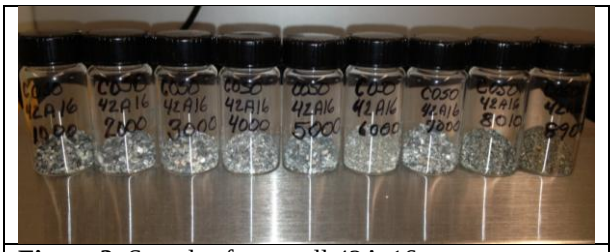

Figure 3: Samples from well 42A-16

wells were sampled:

42A-16 East Flank ~ 10 samples - productive

83-11 West Flank ~10 samples - non productive

56-16 East Flank margin ~10 samples - marginal injector

Navy II West, ~ 7 samples - productive center of the field

These samples were chosen as an initial suite that is reasonably vertically and horizontally representative of the reservoir. Only results from the first of these wells will be discussed in this paper.

ANALYTICAL TECHNIQUES

Neutron Scattering – what and why

The primary techniques used in this study to quantify porosity at scales below approximately 10 microns were small and ultrasmall-angle neutron scattering (U)SANS. (cf. Guinier and Fournet, 1955, Radlinski, 2006, Hammouda, 2009, Anovitz et al., 2009, 2011, 2013). Scattering contrast in rock samples arises primarily from the difference in the coherent scattering length densities (SLD) of the rock and the pores within it. The SLDs of different minerals in the rock are often similar, making

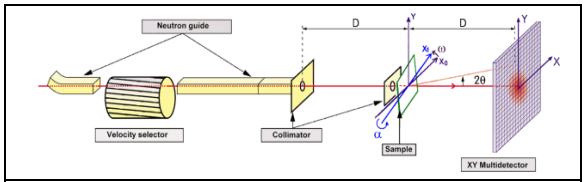

Figure 4: Schematic representation of a SANS experiment showing beam path, sample scattering and detector

their scattering contributions negligible. Thus, (U)SANS analysis provides a direct characterization of pore structure. Neutron beam cross sections are typically several cm^2, and cole neutrons are highly penetrating, compared with photons and electrons. Thus, the scattering curve results from a relatively large, and more statistically meaningful rock volume (typically ~ 30 mm^3, Anovitz et al., 2009). In addition, the high penetrating power of neutrons, relative to X-rays, allows analysis of thicker rock samples by neutron scattering. The SLD of phase j is given by:

$$r_j^* = \sum_{i=1}^{n} b_i \frac{r_j N_A}{M_i} \qquad (1),$$

where b_i is the bound coherent scattering length of atom i, N the total number of atoms in the molecule, ρ_j is the mass density, N_A is the Avogadro constant and M_i is the molar mass. The total neutron scattering cross section for hydrogen is large, allowing studies of water/rock interactions at nano- to micro-scales (and at various time scales with inelastic/ quasi-elastic scattering techniques). In fact, while the scattering cross section for X-rays is a function of the atomic number, that for neutrons is not, thus providing a significantly different, and very

Figure 5: Detector tanks for two SANS instruments at the HFIR. The General Purpose SANS (with tank door open) and the bioSANS (nearer) are shown. The sample positions are at the other end of the tanks (far left).

useful scattering contrast.

Scattering from rocks occurs both from pores that are connected to the overall network and those that are not, and the large difference in SLD between hydrogen and deuterium means that the rock can be saturated with a matrix contrast matched H_2O/D_2O mixture to separate connected from unconnected porosity, allowing a quantitative assessment of the interacting reservoir volume.

A schematic of a pinhole SANS instrument is shown in. **Fig. 4**. Neutrons pass through a velocity selector (monochromator) then down a long guide and collimator. An aperture at the end of the collimator defines the cross section of the neutron beam interacting with the sample. The sample scatters part of the neutrons, and the rest are transmitted or absorbed. The intensity of scattered and transmitted neutrons is measured with 1D or 2D detectors, normalized by the transmission and ce calibrated to absolute intensity. The neutron detector resides in a large, cylindrical vacuum chamber (typically 10-20m long) to reduce interference from air scattering (**Fig**. **5**). The position of the detector and the beam stop can be varied to obtain a wider range of scattering angles. The Q ranges covered by SANS instruments vary somewhat, but are typically in the range from $1*10^{-3} < Q < 0.7$ Å^{-1}, which samples scattering features (e.g. pores) ranging from approximately 10 to 6000 Å.

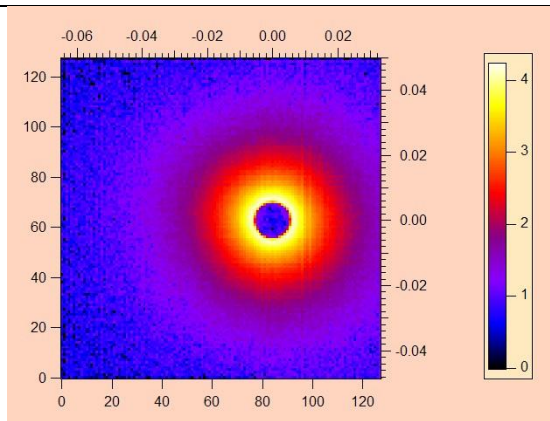

Figure 6: Example scattering data at a single detector distance. Intensities are higher near the direct beam (lower Q, larger scale lengths). Scattering is isotropic for this sample. The center is intentionally offset to increase the Q-range sampled.

The resultant scattering pattern for rocks typically looks like that shown in **Fig**. **6**. This pattern is radially symmetrical if there is no preferred orientation in the sample, and is radially integrated to obtain the scattering curve after appropriate corrections are applied. While the resultant integrated and normalized intensity could be plotted in terms of scattering angle, it is more commonly shown in terms of the momentum transfer vector Q (with units of Å^{-1}), defined as shown in **Fig**. **7**, where Q is the momentum transfer, and E is the energy transfer.

The USANS instrument uses a different design to measure scattering at lower Q. The USANS at NIST/NCNR covers a Q range from $4*10^{-5}$ Å^{-1} < Q < $1*10^{-3}$ Å^{-1}, corresponding to 7.8 μm > d > 628 Å (Hammouda, 2009). Thus, the two techniques are complementary. The USANS uses thermal neutrons (2.4 Å) and the Bonse-Hart method in which neutrons are monochromated by a triple-bounce, channel-cut single-crystal silicon monochromator, passed through the sample to another monochromator and then to a detector. Scanning the analyzer

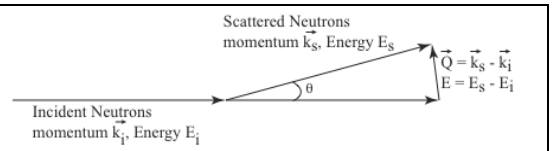

Figure 7: Vector diagram showing the origin of the Q vector.

yields the angular dependence of the scattering intensity. This allows a narrow wavelength resolution (ΔλΔλ = 0.059), but beam intensity is low relative to SANS, making count times longer. In addition, the use of a slit, rather than a pinhole geometry requires desmearing.

Scattering data can be analyzed in reciprocal space by least-square fitting to model functions or in real space after Fourier-transformation. Both techniques yield information about the shape and size or size ranges of scatterers. The invariant Z, defined by

$$Z = \int_0^\infty Q^2 I(Q)\,dQ \qquad (2),$$

yields direct, model-independent information about the scattering contrast and volume of scatterers. For a two-phase system the invariant is given by:

$$Z = 2p^2 f_1 (1 - f_1)(r_1^* - r_2^*)^2 \qquad (3),$$

with ϕ_1 equal to the volume fraction of phase 1 and ρ_1^* its coherent SLD. A great deal of other data can also be obtained from these scattering curves. Once the raw data have been reduced (cf. Kline, 2006), data yield the overall and cumulative porosities, pore distribution geometry (mass fractal behavior), the nature of the pore/rock interface (surface fractal behavior), characteristic lengths associated with the fractal behavior, and the surface area to volume ratio. Information on the pore size

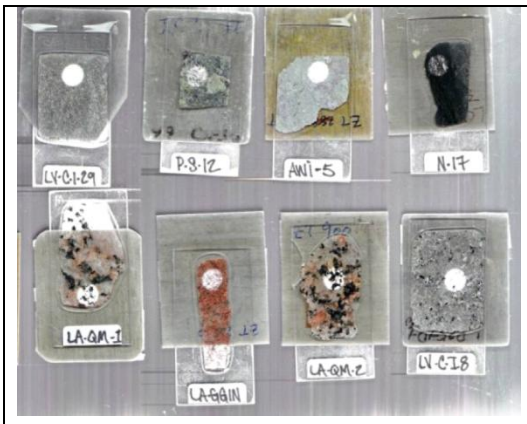

Figure 8: Eight samples from different geothermal fields ground to 150 microns thick and polished on quartz glass plates with Cd masks.

distribution and connectivity provides key insight into capillary pressure behavior and liquid storage in the reservoir. In many cases, even the combination of SANS and USANS does not cover a sufficiently large Q range to describe the complete scattering curve for many rocks. There are several approaches to filling this gap, including backscattered electron (SEM/BSE) imaging (Radlinski et al., 2004, Anovitz et al., 2013). We have developed an autocorrelation approach based on this kind of imaging and intend to both use and X-ray CT images as part of this study (see below).

While neutrons are very penetrating, suitable sample thickness is important. If the sample is too thin, scattering power will be low. If too thick, multiple scattering lowers scattering intensity at low Q and raises it at higher Q, distorting the signal. Anovitz et al. (2009) showed that, for limestone samples, a thickness of 150 microns was suitable. We typically prepare samples by mounting them on quartz glass plates 1mm thick (Anovitz et al., 2009). Examples of such samples from several geothermal fields, mounted on cadmium masks, are shown in **Fig**. **8**. Such samples were not available from the Coso wells; however, well cuttings cast into epoxy blocks and then sectioned were used, although this limits the availability of information on porosity at the largest (cm) scales.

Neutron scattering has the advantage over high magnification imaging techniques of providing statistically meaningful characterizations averaged over large volumes of material. While electron microscopy can provide detailed images of pores at high magnifications, the total volume of the rock imaged is, of necessity, very small. In fact, Howard and Reed (2005) calculated that if all the material that has ever been in focus in all of the transmission electron microscopes in the world were gathered together it would total less than 1 cm^3. At lower magnifications, however, imaging techniques can be used to extend the range of scattering data from ~ 10 microns to ~ 1 cm using backscattered electron imaging with SEM, or X-ray computed tomography. This is done, following the work of Debye et al. [1957], Radlinski et al.(2004) and Anovitz et al. (2013) by calculating the autocorrelation curve from such images, providing a further extension of the scattering curve. Together, these techniques provide quantitative characterization of rock porosity at scales ranging from ~ 1 nm to greater than 1 cm – 7 orders of magnitude.

Neutron scattering data were obtained at three facilities. SANS data at the highest Q-range (smallest scales) were obtained using the LQD instrument at the Los Alamos Neutron Science Center (LANSCE), at the Los Alamos National Laboratory, New Mexico. Intermediate Q-range data were obtained using the KWS III VSANS Instrument at the Forschungs - Neutronenquelle Heinz Maier-Leibnitz (FRM II), Technische Universität München, Munich, Germany, and low-Q range data from the BT-5 USANS instrument at the NIST Center for Neutron Research in Gaithersburg, MD (Hammouda, 2009).

Image Processing QEMSCAN and XRD

Three samples from depths 1000, 7000, and 8900 feet of the Coso Navy II well 42A-16 were chosen for SEM and powder X-ray diffraction analysis. The same thick sections that were subjected to neutron scattering experiments were carbon coated and imaged using an FEI Quanta 250 FEG SEM at 25 keV accelerating voltage and large spot size (6.81) with the electron source tilted to achieve a 10 nA specimen current. The Quanta FEG is equipped with the FEI QEMSCAN analytical platform that includes a high-speed silicon drift X-ray detector and iDiscover 5.2 software. The point spacing for analysis was set to 2.5 microns,

producing a mineral map of approximately 2.5 micron pixel resolution. At each point, 1000 counts of characteristic X-rays were acquired, as well as a backscattered electron signal intensity, and those experimental data were compared to a list of mineral standards prepared by FEI. For each thick section, an approximate 4 x 4 mm area was analyzed. The standard list was subsequently grouped based on textural analysis of the sample while still in the QEMSCAN sample holder. In general, mineral identifications of only a few pixels in dimension were either classified as unknowns (others) or grouped with another mineral standard of appropriate chemistry as deemed reasonable by checking the grain shapes in the SEM. In addition, some manual EDS spot analyses were acquired. Powder X-ray diffraction scans were obtained from hand-ground and back-loaded specimen mounts using a PANalytical ExpertPro X-ray diffractometer, HighScore Plus software, and the PDF 4+ database. The X-ray scans were utilized to help verify mineral identifications from the SEM.

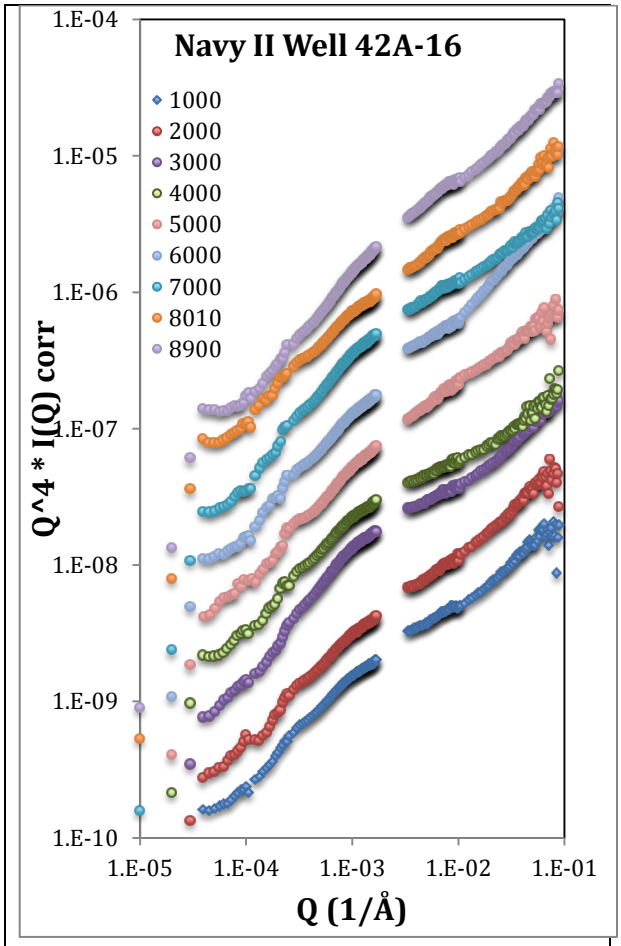

Figure 9:Porod-transformed, offset neutron-scattering data for samples from Navy II Well 42A-16 at depths from 1000 to 8900 feet.

RESULTS

Fig. 9 shows the Porod-transformed, offset scattering data for the samples from Navy II well 42A-16. It is clear from these data that the pore structure of this rock cannot be described as a simple surface fractal, nor as a combination of surface and mass fractal behavior. (cf. Anovitz et al., 2009, 2010, 2013). Instead, there is a steep surface-fractal like background that increases slightly, but not completely monotonically with depth (2.79 at 1000 feet, 2.71 at 4000 feet, 2.86 at 8900 feet) that appears to decrease, implying smoother surfaces at the largest scales for the deeper samples, modified by a pore structure of

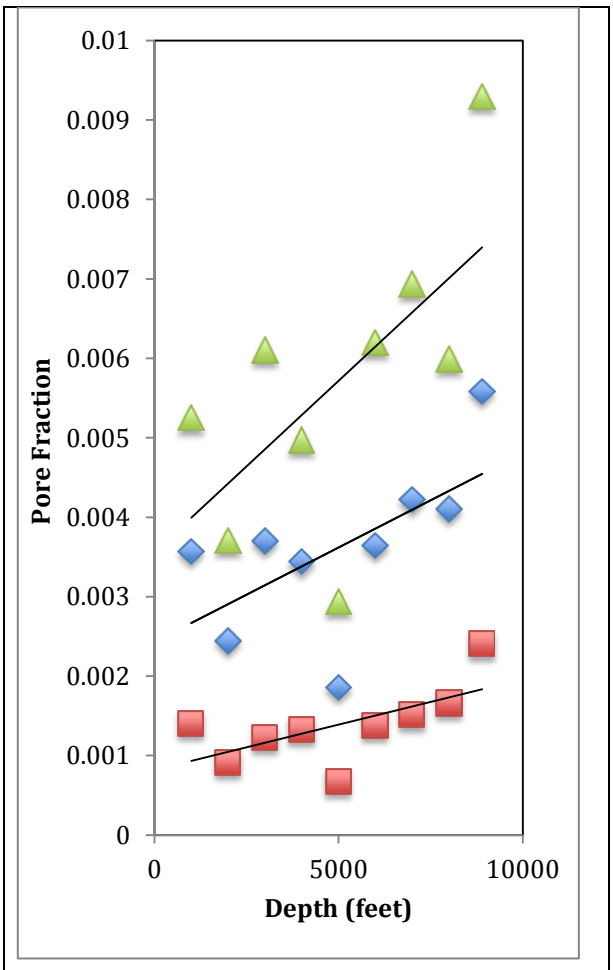

Figure 10: Total scattering porosity (green triangles), and pore fractions

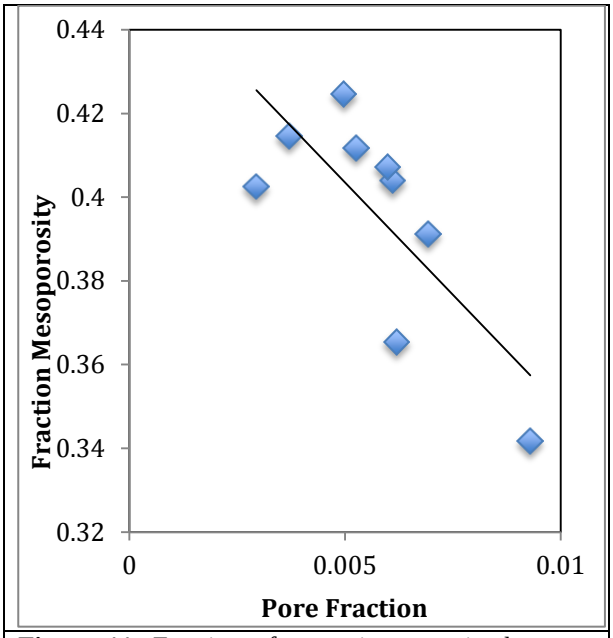

Figure 11: Fraction of scattering porosity between 10^4 and 10^5 Å as a function of total pore fraction. As the overall porosity increases, the fraction of mesoporosity decreases.

varying intensity in the mid-Q region. These observed fractal dimensions likely represent a combination of actual pore surface roughness and a fractal distribution of pore sizes.

As shown in **Fig. 10** and **Fig. 11**, the porosities at all scales generally increase with depth, but the fraction of mesoporosity (defined here as pores with radii between 10^4 and 10^5 Å), reflecting a shift in the "hump" in the middle of the scattering curve, decreases with increasing porosity. It is further clear from these data that the porosity of these rocks at scales observed by neutron scattering (approximately 1 nm to 10 microns) is quite small (< 1 %). These data also suggest a significant change in the values for the deepest sample. This correlates well with the color change obvious in **Fig. 3** at 8900 feet.

Fig. 12 shows the pore volume as a function of pore radius, calculated from the scattering curves for the 1000 foot and 8900 foot samples. As can be seen, the pore volumes are bimodal, with a break somewhere between 10^4 and 10^5 angstroms. In addition, while the pore volumes at all scales increase with depth as suggested in **Fig. 10**, there is also an increase in the relative pore volumes at smaller scales.

The nature of the internal pore morphology and its chemical reactivity are, ultimately controlled by the mineralogy of the rock in question and the degree which the porosity is accessed by the existing fracture network and it's complexity. **Figs. 13 - 15** show the QEMSCAN images of the mineralogy of samples from 1000, 7000, and 8900 feet. Major

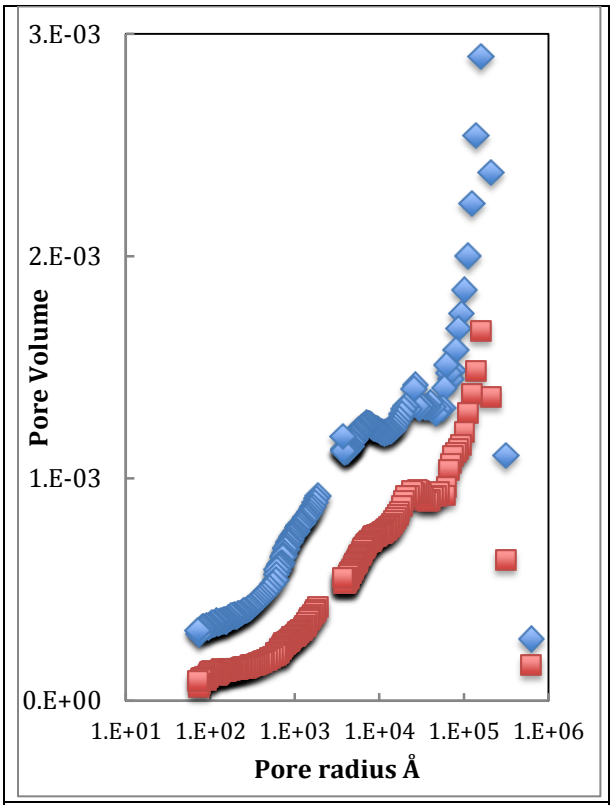

Figure 12: Pore volume as a function of pore radius for the 1000 foor sample (red) and the 8900 foot sample (blue). Note the increase in overall porosity, and shift to smaller pores with depth. Curves are not offset.

minerals common to all three samples include plagioclase, potassium feldspar, biotite mica, and amphibole (**Table 1**). Minor constituents common to all are titanite (sphene), chlorite, and epidote. Both SEM and XRD data suggest that Fe-oxides are most abundant in Coso 8900 (**Fig. 15**). XRD pattern matching suggests the presence of Fe-oxide (magnetite) only in Coso 8900; QEMSCAN of the 7000 foot sample shows only minor Fe-oxide, and negligible quantities are observed in the 1000 foot sample. QEMSCAN and BSE mapping show that the Fe-oxides are complex, often displaying a porous, layered texture that is at least partly silicified, as verified by manual EDS spot analysis. This suggests that magnetite likely altered to goethite or other Fe-hydroxide phases.

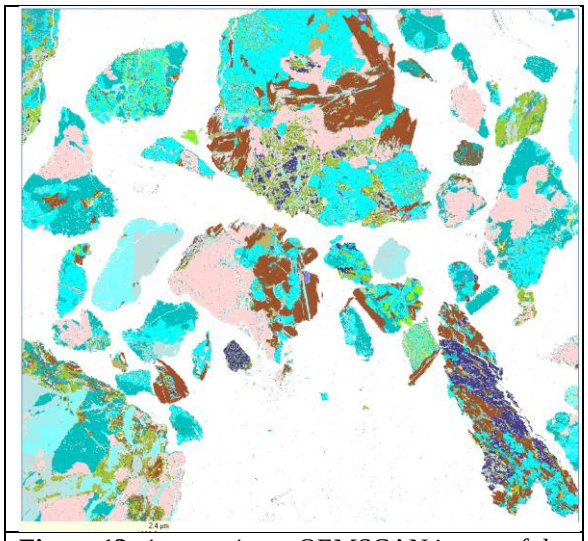

Figure 13: 4 mm x 4 mm QEMSCAN image of the mineralogy of the 1000 foot sample. Colors as follows: white – mounting plastic, pink – quartz, light blue – calcite, medium light blue – plagioclase, medium dark blue – K-feldspar, purple – amphibole, dark brown – biotite, medium brown and tan – goethite, hematite limonite, other Fe oxides/ hydroxides, dark green – chlorite, light green – epidote, brownish green – titanite.

It is clear from these data that a significant part of the pore changes observed are related to alteration of the granite. The 1000-foot sample shows a significant fraction of calcite replacement. Chlorite - epidote (propylitic) alteration, most closely associated with plagioclase and biotite, is apparently most extensive in the Coso 8900 foot sample (**Fig. 15**; **Table 1**), but this QEMSCAN result is not verified by XRD. Chlorite occurs as a replacement mineral for biotite and amphibole, sometimes forming intricate veins that crosscut the original mineral in more than one orientation. This alteration texture is most pronounced in amphibole grains of the Coso 1000 foot sample (**Fig. 13**). In addition, XRD observations suggest that calcite is most abundant in the Coso 1000 foot sample; this is consistent with the QEMSCAN mineral map (**Fig. 13**) that shows calcite veins crosscutting several "primary" phases, most notably biotite, amphibole, and plagioclase feldspar. Intra-grain fractures partially infilled with chlorite or calcite alteration seem most common in the Coso 1000 foot and 7000 foot samples, but more extensive textural analysis of larger regions of the Navy II 42A-16 well cuttings is required to substantiate this observation.

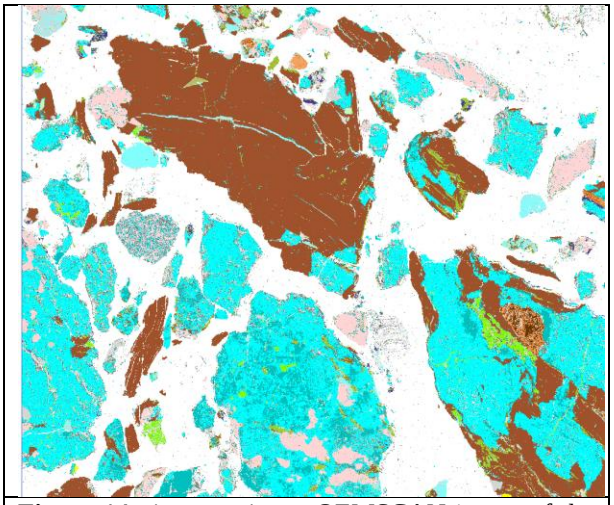

Figure 14: 4 mm x 4 mm QEMSCAN image of the mineralogy of the 7000 foot sample. Colors as in **Fig. 13**.

DISCUSSION

Well 42A-16 was completed in January, 2009 as an east flank production well. The well has a slotted liner from 5823 to 9134 feet measured depth. No static temperature or pressure survey data are available prior to the well being placed on production. A detailed pressure/temperature/ spinner (P/T/S) survey performed after a few months production identified production entries

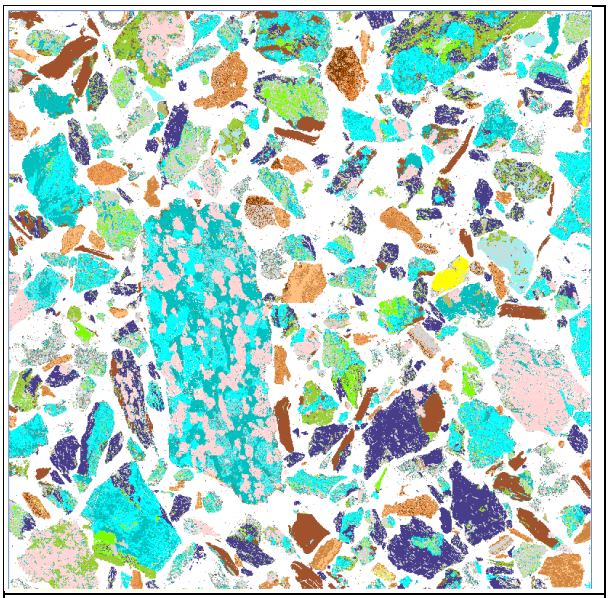

Figure 15: 4 mm x 4 mm QEMSCAN image of the mineralogy of the 8900 foot sample. Colors as in **Fig. 13**.

Table 1: Summary of mineral percentages (by area) determined from QEMSCAN analysis			
	1000 foot	7000 foot	8900 foot
Mineral	Area %	Area %	Area %
Amphibole	4.16	2.96	14.29
Apatite	0.29	0.00	0.00
Biotite	12.30	27.40	6.69
Calcite	6.70	1.13	0.66
Chlorite	5.60	2.51	5.18
Epidote	1.55	1.31	3.73
Goethite	0.06	0.51	1.98
Hematite	0.03	0.25	0.63
K-Feldspar	16.45	7.23	11.08
Limonite	1.06	0.59	3.38
Magnetite	0.01	0.23	0.61
Plagioclase	18.63	27.90	16.55
Pyrite	0.01	0.21	0.52
Quartz	16.73	13.41	11.77
Sphene	1.15	0.22	0.66
Misc	15.27	14.15	22.28

8200 to 8350 feet and 8900 to 9000 feet, with the first set of entries producing two-thirds of the total fluid. The production along the long slotted liner has production near the bottom concentrated in a total interval of 250 feet out of over 3300 feet of reservoir exposure. The well initial potential was approximately 600 Klbm/hr with transient flow lasting for over 1000 hours. Well productivity is comparable to other medium sized east flank wells. The production rate-time, when plotted in a log-log format, clearly shows a half-slope response, diagnostic of a linear or fracture flow regime.

The well description, neutron scattering and QEMSCAN provide a view of a geologically recent, deep thermal reservoir with better developed matrix porosity at depth than shallower in the well, with most porosity development below 8000 ft, in agreement with the production P/T/S response. The east flank geothermal reservoir at Coso is a younger thermal feature than the main field. Recent northward extension of the Coso Wash fault and vertical displacement has allowed deep thermal fluid to charge the fault.

The 42A-16 location is in an older portion of the Coso Wash fault, approximately two miles south of the hot springs, and thus has had sufficient geologic time to develop additional fracture complexity compared to more northerly production wells. **Fig. 10** shows the impact of fault development and growth on creating porosity, with greater porosity at depth. There seems to be a region between 1000 to 50000 Å where there is greatest separation between the two depths. This may suggest the deeper, hotter system upwelling from depth preferentially created porosity in this pore size range by the dissolution of amphibole, plagioclase, biotite, calcite, quartz and k-feldspar. The pattern of increasing effective porosity with depth is opposite to hydrocarbon reservoirs where porosity typically decreases with depth, impacting fluid storage distributions. The alteration, however, is similar to that observed in porphyry copper, and other fossil hydrothermal systems (Rose and Burt, 1979; Beane, 1982; Beane and Titley, 1981).

Drilling data, well P/T/S surveys, production well flow regimes, and tracer returns demonstrate deep fracturing with temperatures approaching 640°F in this region of the reservoir. The porosity measured show the impact rock/water interactions have developing a more connected micro-porosity system. A better understanding of the impact of time on porosity development may come from studying other well cutting samples at Coso for spatial patterns.

The pore morphology characterized by the neutron scattering experiments provides a detailed statistical description of the pore size distribution. This information can be used to construct a theoretical capillary pressure curve for the reservoir rock. Spatial differences in the capillary pressure in the reservoir may have implications for relative differences in fluid storage and for reinjection locations yielding maximum contact with the rock for heat exchange on a flow path back to a production well. Neutron scattering measurements and construction of a capillary pressure curve may compliment laboratory-derived steam-water petrophysical measurements for an improved understanding of fluid storage in geothermal reservoirs.

ACKNOWLEDGEMENTS

Research supported by the Geothermal Technologies Office, Office of Energy Efficiency and Renewable Energy, U.S. Department of Energy under contract DE-AC05-00OR22725, Oak Ridge National Laboratory, managed and operated by UT-Battelle, LLC. We acknowledge the support of the National Institute of Standards and Technology, Center for Neutron Research, U.S. Department of Commerce, and the High-Flux Isotope Reactor at the Oak Ridge National Laboratory in providing the research neutron facilities used in this work. This work utilized facilities supported in part by the National Science Foundation under agreements nos. DMR-0454672 and. DMR-0944772. Certain commercial equipment, instruments, materials and software are identified in this paper to foster understanding. Such identification does not imply recommendation or endorsement by the National Institute of Standards and Technology, the Department of Energy, or the Oak Ridge National Laboratory, nor does it imply that the materials or equipment identified are necessarily the best available for the purpose. This work is based upon experiments performed at the QWS III instrument operated by JCNS at the Forschungs-Neutronenquelle Heinz Maier-Leibnitz (FRM II), Garching, Germany. This work has benefited from the use of the Manuel Lujan, Jr. Neutron Scattering Center at Los Alamos National Laboratory, which is funded by the Department of Energy's Office of Basic Energy Sciences. Los Alamos National Laboratory is operated by Los Alamos National Security LLC under DOE Contract DE-AC52-06NA25396. Measurements of the mineralogy and mineral distributions were carried out in the Subsurface Energy Materials Characterization and Analysis Laboratory (SEMCAL) at OSU. We would also like to thank Jess McCulloch and Coso Operating for their help and assistance and providing samples.

REFERENCES

Adams, M.C., Moore, J.N., Bjornstad, S., Norman, D.I. (2000) Geologic history of the Coso geothermal system. Geothermal Resources Council Transactions 24, 205–209.

Ague, J. J. (2004) Fluid flow in the deep crust. In. Treatise of Geochemistry, Vol. 3 The Crust, R. L. Ridnick (ed.), 195-228.

Anovitz, LM, Lynn, GW, Cole, DR, Rother, G, Allard, LF Jr., Hamilton, WA, Porcar, L, and Kim, M-H (2009) A new approach to quantification of metamorphism using ultra-small and small angle neutron scattering. Geochim. Cosmochim. Acta 73, 7303-7324.

Anovitz, LM, Rother, G, and Cole, DR (2011) Characterization of rock pore features in geothermal systems using small angle neutron scattering (SANS). Proc. 36th Workshop on Geothermal Reservoir Engineering, SGP-TR-191, 571-582.

Anovitz, LM, Cole, DR, Rother, G, Allard, LF JR., Jackson, A, and Littrell, KC (2013) Diagenetic changes in macro-to nano-scale porosity in the St/ Peter Sandstone: an (Ultra) small angle neutron scattering and backscattered electron imaging analysis. Geochim, Cosmochim. Acta, 102, 280-305.

Beane, RE (1982) Hydrothermal alteration in silicate rocks. In: Advances in Geology of Porphyry Copper Deposits, Southwestern North America, SR titley, ed. University of Arizona Press, Tucson, 117-137.

Beane, RE and Titley, SR (1981) Porphyry copper deposits. Part II. Hydrothermal alteration and mineralization, Econ, Geol. 75th Anniv. Vol., 2235-269.

Debye P, Anderson, Jr., HR and Brumberger H (1957) Scattering by an inhomogeneous solid. II. The correlation function and its application. J. Appl. Phys. 28, 679–683.

Deutch, J. and Moniz, E. J. (2007) The Future of Coal. Options for a Carbon-Constrained World. An Interdisciplinary MIT Study. p. 51, Massachusetts Institute of Technology.

DOE-EGS (2006) The Future of Geothermal Energy: Impact of Enhanced Geothermal Systems (EGS) on the United States in the 21st Century. http://www1.eere.energy.gov/geothermal/egs_technology.html

Guinier, A and Fournet, G (1955). Small Angle Scattering of X-rays. New York: John Wiley.

Hammouda, B (2009) Probing Nanoscale Structures. The SANS Toolbox, book available online at http://www.ncnr

.nist.gov/staff/hammouda/the_sans_toolbox.pdf

Ingebritsen, S. E. and Sanford, W. E. (1999) Groundwater in Geologic Processes. Cambridge University Press, 341 pg.

Johnson, J. W., Nitao, J. J., and Knauss, K. G. (2004) Reactive transport modeling of CO_2 storage in saline aquifers to elucidate fundamental processes, trapping mechanisms and sequestration partitioning. In: *Geological Storage of Carbon Dioxide* (S. J. Barnes and R. H. Worden, eds.) Geological Society, London Spec. Pub. 233, 107-128.

Kline SR (2006) Reduction and analysis of SANS and USANS data using IGOR Pro. J. Appl. Crystallogr. 39, 895–900.

Kurilovitch, L., Norman, D., Heizler, M., Moore, J., McCulloch, J., 2003. 40Ar/39Ar thermal history of the Coso geothermal field. In: Proceedings of the Twenty-Eighth Workshop on Geothermal Reservoir Engineering, Stanford University, pp. 110–116.

Manley, C.R., Bacon, C.R., 2000. Rhyolite thermobarometry and the shallowing of the magma reservoir, Coso Volcanic Field, California. J. Petrology 41, 149–174.

McClusky, S.C., Bjornstad, S.C., Hager, B.H., King, R.W., Meade, B.J., Miller, M.M., Monastero, F.C., Souter, B.J., 2001. Present day kinematics of the eastern California shear zone from a geodetically constrained block model. Geophys, Res. Let. 28, 3369–3372.

Newman, GA, Gasperikova, E., Hoversten, GM, and Wannamaker, PE (2008) Three-dimensional magnetotelluric characterization of the Coso geothermal field. Geothermics 37, 369-399.

Norton, D. (1979) Transport phenomena in hydrothermal systems: the redistribution of chemical components around cooling plutons. Bull. Mineral. 102, 471-486.

Norton, D. and Knapp, R. (1977) Transport phenomena in hydrothermal systems: the nature of porosity. Amer. J. Sci. 277, 913-936.

Radlinski, AP (2006) Small-angle neutron scattering and rock microstructure. In: Neutron Scattering in Earth Sciences, ed. by H-R Wenk, Reviews in Mineralogy and Geochemistry 63, 363-397.

Radlinski, AP, Ioannidis, MA, Hinde, AL, Hainbuchner, M, Baron, M, Rauch, H, and Kline, SR (2004) Angstrom-to-millimeter characterization of sedimentary rock microstructure. J. Colloid Interface Sci 274, 607-612.

Roquemore, G. (1980) Structure, tectonics, and stress field of the Coso Range, Inyo County, California. J. Geophys. Res. 85, 2434–2440.

Rose, AW, and Burt, DM (1979) hydrothermal alteration. In: Geochemistry of Hydrothermal Ore Deposits, 2nd ed., HL Barnes, ed. John Wiley and Sons, New York, 173-235.

Whitmarsh, R.S., 2002. Geological map of the Cactus Peak 7.5_ quadrangle, Inyo County, California, CD-ROM map. In: Glazner, A.F., Walker, J.D., Bartley, J.M. (Eds.), Geologic Evolution of the Mojave Desert and Southwestern Basin and Range. Geol. Soc. Amer. Mem., p. 195.